X-ray diffraction contrast tomography in micro-CT lab source systems

Wim van Aarle
Wolfgang Ludwig

INSAVALOR
(on behalf of European Synchrotron Radiation Facility)
66, BOULEVARD NIELS BOHR
VILLEURBANNE 69100 FRANCE

Report Date: May 2014

Final Report from 15 March 2013 to 14 March 2014

Air Force Research Laboratory
Air Force Office of Scientific Research
European Office of Aerospace Research and Development
Unit 4515, APO AE 09421-4515

REPORT DOCUMENTATION PAGE

1. REPORT DATE *(DD-MM-YYYY)*	2. REPORT TYPE	3. DATES COVERED *(From – To)*
16 May 2014	Final Report	15 March 2013 – 14 March 2014

4. TITLE AND SUBTITLE

X-ray diffraction contrast tomography in micro-CT lab source systems

5a. CONTRACT NUMBER

FA8655-13-1-3059

5b. GRANT NUMBER

Grant 13-3059

5c. PROGRAM ELEMENT NUMBER

61102F

6. AUTHOR(S)

Wim van Aarle
Wolfgang Ludwig

5d. PROJECT NUMBER

5d. TASK NUMBER

5e. WORK UNIT NUMBER

7. PERFORMING ORGANIZATION NAME(S) AND ADDRESS(ES)
INSAVALOR (on behalf of European Synchrotron Radiation Facility)
66, BOULEVARD NIELS BOHR
VILLEURBANNE 69100 FRANCE

8. PERFORMING ORGANIZATION REPORT NUMBER

N/A

9. SPONSORING/MONITORING AGENCY NAME(S) AND ADDRESS(ES)

EOARD
Unit 4515
APO AE 09421-4515

10. SPONSOR/MONITOR'S ACRONYM(S)

AFRL/AFOSR/IOE (EOARD)

11. SPONSOR/MONITOR'S REPORT NUMBER(S)

AFRL-AFOSR-UK-TR-2014-0023

12. DISTRIBUTION/AVAILABILITY STATEMENT

Distribution A: Approved for public release; distribution is unlimited.

13. SUPPLEMENTARY NOTES

14. ABSTRACT

In this work we have developed an efficient projector for laboratory based, polychromatic cone beam diffraction imaging. Using this projector, the three-dimensional shape of grains with negligible intra-granular orientation gradient can be reconstructed using iterative, algebraic reconstruction techniques (e.g. SIRT). The reconstructions show a clear improvement compared to the previously used processing route, based on a regular cone beam projector and affine transformation of the projection images. With further improvement of polycrystalline indexing algorithms and with extension to a 6D reconstruction framework, we anticipate LabDCT to become a true alternative to established synchrotron techniques. The combination of absorption (detection of damage, second phases, porosity, plastic strain via 3D digital volume correlation techniques) and diffraction imaging (crystal shape and orientation, elastic strain) on the same instrument will provide unique possibilities for (interrupted) in-situ characterization of dynamic processes in the bulk of polycrystalline materials (e.g. grain coarsening during heat treatment, plastic deformation and damage mechanisms, etc.)

15. SUBJECT TERMS

EOARD, diffraction contrast tomography, 3D materials characterization

16. SECURITY CLASSIFICATION OF:			17. LIMITATION OF ABSTRACT	18, NUMBER OF PAGES	19a. NAME OF RESPONSIBLE PERSON
a. REPORT	**b. ABSTRACT**	**c. THIS PAGE**			Lt Col Randall Pollak
UNCLAS	UNCLAS	UNCLAS	SAR	19	**19b. TELEPHONE NUMBER** *(Include area code)* +44 1895 616115, DSN 314-235-6115

Standard Form 298 (Rev. 8/98)
Prescribed by ANSI Std. Z39-18

FINAL REPORT

16 May, 2014

X-ray diffraction contrast tomography in μCT lab source systems

---

Project Team:

W. van Aarle[1], and **W. Ludwig**[2]

[1] wim.vanaarle@uantwerpen.be
[2] wolfgang.ludwig@esrf.fr

USA Collaborator:

D. Penumadu

dpenumad@utk.edu

Program Manager:

Dr. Randall 'Ty' Pollak, Lt Col, PhD

International Program Officer
EOARD Materials & Nanotechnology
Office: +44-1895616115 (DSN 314-235-61)

1

Progress Report

1.1 Introduction

X-ray diffraction contrast tomography (DCT) is a nondestructive characterization method providing access to the three-dimensional grain microstructures in a wide range of polycrystalline materials. DCT is a truly three-dimensional tomographic imaging approach, sharing a common experimental setup with conventional X-ray microtomography. After interaction with the material, both the transmitted and diffracted beams are recorded on a high-resolution X-ray imaging detector positioned close to the sample. The three-dimensional distribution of the X-ray attenuation coefficient, and the three-dimensional shape, grain average orientation and elastic strain tensor of all grains in the illuminated sample volume, are determined from analysis of the transmitted and diffracted intensities, respectively

DCT analysis of polycrystalline materials is currently a hot topic at synchrotron radiation facilities around the globe. The monochromatic nature of a synchrotron beam, its parallel beam geometry, and its high spatial resolution make it an ideal imaging modality to measure three-dimensional grain microstructures in a wide range of polycrystalline materials. The combination of three-dimensional X-ray imaging and diffraction techniques on the same instrument are particularly interesting for the study of deformation and damage mechanisms in structural materials [1, 2, 3], but current applications cover a much wider spectrum, including phase transformations and grain coarsening processes.

Fig. 1.1 showcases the combined use of (synchrotron) X-ray phase contrast and X-ray diffraction contrast tomography for characterization of fatigue crack propagation in metal alloys. The 3D dimensional grain microstructure of a bcc Ti alloy sample has been mapped out with DCT prior to an in-situ fatigue experiment carried out on the same specimen. The combined characterization enables characterization and interpretation of crack orientation and crack growth rate as a function of local crystallographic orientation [2].

However, given the high operating cost and their limited availability, synchrotron facilities often do not provide a feasible solution. It would, therefore, be very beneficial if DCT imaging were to be possible on conventional table-top μCT systems that are relatively cheap and more widely available. The downside of such a lab source CT system is its cone beam geometry and the polychromatic nature of its X-ray source. This results in complicated software simulations of diffraction projections (and thus also their reconstruction), which are difficult to implement efficiently on modern computational infrastructure such as GPU's.

In this work, an accurate and efficient projection model is introduced for the case of polychromatic cone beam DCT. In Section 1.2, the forward and backprojection model of this projector is mathematically introduced and its efficient implementation is discussed. Subsequently, in Section 1.3, these projectors are used to reconstruct a grain of an Aluminium Copper microstructure, scanned in a μCT system. Section 1.4, finally, concludes this work and provides an outline into future research directions that could greatly benefit the application of DCT in lab source systems.
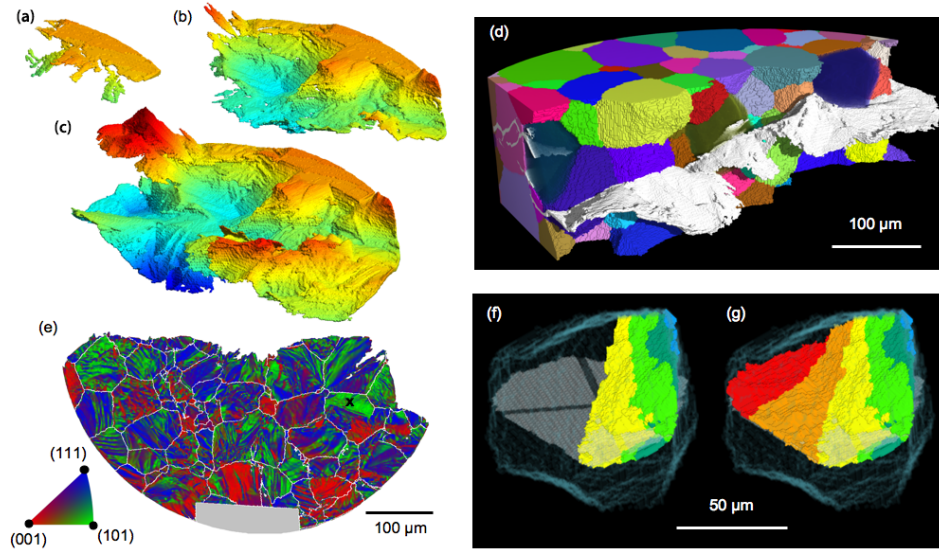
Figure 1.1: **(a-c)** 3D rendition of a fatigue crack in a Ti alloy reconstructed from phase contrast tomography (PCT) after 46, 61 and 75 *103 loading cycles. The color corresponds to the vertical crack position. **(d)** 3D rendition of the combined data set showing the crack and the surrounding 3D grain microstrucutre as determined from DCT. **(e)** Surface mesh representing the fracture surface, colour coded with respect to its crystallographic orientation. Grain boundaries are labelled in white. **(f,g)** Crack propagation within the grain labelled in (e). The activated (110) slip plane and the two (111) slip directions are highlighted in gray and black, respectively.

1.2 Cone beam dct projector

In this section, a projector is introduced that simulates the diffraction images of grains in a lab source cone beam μCT-system. We assume that the diffraction spots have already been indexed and that for each of the grains the center of mass and crystallographic orientation has been determined. For details on the indexing procedure for polychromatic DCT data we refer to the article by [4]. Note that the number of projection images per grain depends on material and experiment parameters but is typically of order of one hundred.

In Section 1.2.1, necessary notation is introduced regarding the volume and projection geometry of polychromatic cone beam diffraction contrast tomography (henceforth referred to as *LabDCT*). Section Section 1.2.2 and Section 1.2.3 subsequently introduce the back- and forward projection respectively. Finally, in Section 1.2.4, we discuss some implementation details that were required to optimise to projector performance.

For the sake of readability, we refrain from delving too deep into the mathematics of the projection models. Instead, we refer to Appendix A where more in-depth derivations are provided for many of the formulas presented in this section.

1.2.1 Notation

Any tomographic projection model is defined by both a volume geometry, defining the reconstruction volume, and a projection geometry, defining the trajectory and orientation of the X-ray source and detector[1] with respect to the volume. In Fig. 1.3, a schematic overview is given of a lab source CT system for diffraction tomography.

For the volume geometry, define n as the total number of voxels and $\Delta v \in \mathbb{N}$ as the voxel length per direction. For simplicity's sake, we assume isotropic voxels.

---

[1] In the remainder of the presentation we will refer to individual detector pixels as *detectors* and we will use the term *detector system* when referring to the full array (2048x2048 elements) of detectors.
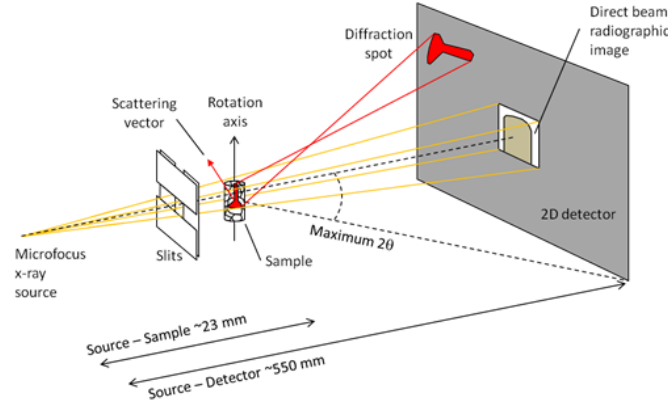
Figure 1.2: Schematic showing the laboratory DCT setup. The technique, originally developed for the case of a monochromatic, parallel synchrotron beam can be adapted to conventional X-ray laboratory tomography scanners with minimal modifications: a set of adjustable slits is inserted between source and sample.
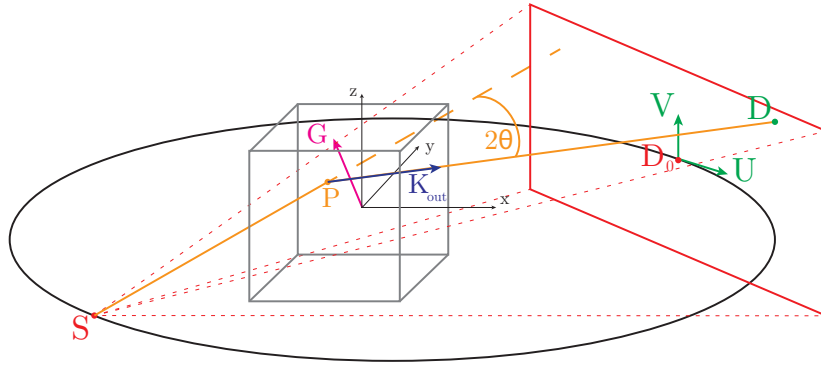

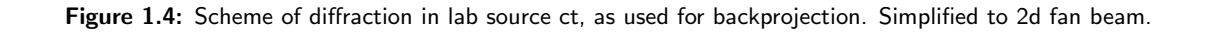**Figure 1.3:** Schematic overview of a 3D cone beam diffraction tomographic geometry.

For the projection geometry, we define m as the total number of detectors per projection and l as the total number of projections. The total number of measurements is then $\bar{m} = ml$. Let $\Delta t \in \mathbb{R}$ denote the width and height of the square detectors. Each projection is defined by a set of five vectors: let $S \in \mathbb{R}^3$ denote the position of the source point, $D_0 \in \mathbb{R}^3$ the position of the centre of the detector plane, $U \in \mathbb{R}^3$ the unit vector that defines the x-dimension of a detector ($\|U\| = \Delta t$), $V \in \mathbb{R}^3$ the unit vector that defines the y-dimension of a detector ($\|V\| = \Delta t$), and $G \in \mathbb{R}^3$ the grain lattice plane normal giving rise to the diffraction spot. Note that any detector point can be expressed by $D = D_0 + t_1 U + t_2 V$ with $t_1, t_2 \in \mathbb{N}$.

1.2.2 Backprojection

For the backprojection operation in LabDCT, only a voxel-driven projection approach can result in the fastest implementations. This means that for each voxel centred at point P, and for each projection image defined by S and D_0, we must simulate the diffraction of the incoming ray and compute the intersection D of the diffracted ray with the detector plane (see Fig. 1.4). Let the inverse incoming ray be defined by the vector $K_{in} = P - S$. Given the law of ray reflection, the outgoing ray, K_{out} can then found by

$$K_{out} = 2G(G \cdot -K_{in}) + K_{in}. \tag{1.1}$$

The equivalence of Eqn. 1.1 to Bragg's law is given in Appendix A.

Figure 1.4: Scheme of diffraction in lab source ct, as used for backprojection. Simplified to 2d fan beam.

The detector D can then be found by computing the intersection between the outgoing ray and the detector plane:

$$P + sK_{out} = D = D_0 + t_1U + t_2V, \tag{1.2}$$

where $s, t_1, t_2 \in \mathbb{R}$ can be found by solving

$$\begin{pmatrix} K_{out,x} & -U_x & -V_x \\ K_{out,y} & -U_y & -V_y \\ K_{out,z} & -U_z & -V_z \end{pmatrix} \begin{pmatrix} s \\ t_1 \\ t_2 \end{pmatrix} = \begin{pmatrix} D_{0_x} - P_x \\ D_{0_y} - P_y \\ D_{0_z} - P_z \end{pmatrix}. \tag{1.3}$$

Detailed information on how to efficiently solve Eqn. 1.3 can be found in appendix A.

1.2.3 Forward projection

Here, a forward projection operator is discussed for use in LabDCT. For computational reasons, forward projecting requires a ray-driven projector. Given a certain detector point, we must thus figure out which voxels in the volume contribute exactly how much to it. For conventional absorption CT, this is easy to figure out as all contributing points lie on a straight line. Rather, for diffraction tomography, these points (i.e. those in which the incoming ray diffracts exactly into the direction of the detector) are on a curved line (henceforth referred to as the *diffraction curve*), requiring more complicated projection equations.

In Section 1.2.3.1, we will introduce formulas that define the diffraction curve for the special case where the source and a given detector are on the x-axis of a 2-dimensional coordinate system, and are located such that their distance to the origin is equal. Given these severe restrictions, we can make use of the property of ellipses saying that any ray originating in one focal point, reflecting on the edge of the ellipse, will end up in the other focal point.

Subsequently, in Section 1.2.3.2, a transformation formula is introduced that allows the special ellipse-based diffraction curve to be used in a general 3D LabDCT cone beam setting.
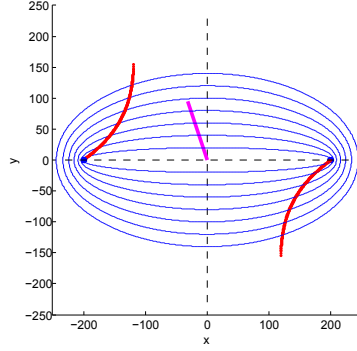
Figure 1.5: A subset of the ellipses with their centre in the origin and with fixed focal points $f = \pm 200$. The thick red line connects all points on these ellipses where the corresponding tangent line is perpendicular to the plane normal (the pink line).

1.2.3.1 Ellipse diffraction model

Consider the set of ellipses with its centre in the origin, their axes aligned with those of the Cartesian grid and with fixed focal points $\pm f$ with $f^2 = a^2 - b^2$ and $0 \le b < a$.

$$\frac{x^2}{a^2} + \frac{y^2}{b^2} = 1. \tag{1.4}$$

Given the in depth derivation given in appendix A, we can see that all points x, y that lie on such an ellipse and whose tangent line at that point of the ellipse is perpendicular to the diffraction normal G, can be described as a function of a:

$$x = \pm \frac{a^2 |G_x|}{\sqrt{a^2 - f^2 G_y^2}}, \quad y = \pm \frac{\text{sgn}(G_x) b^2 G_y}{\sqrt{a^2 - f^2 G_y^2}}. \tag{1.5}$$

The diffraction curve can also be described as a function of x:

$$y = \frac{G_y}{G_x} x - \frac{2 f^2 G_x G_y}{x \pm \sqrt{x^2 - 4 f^2 G_x^2 G_y^2}}. \tag{1.6}$$

In Fig. 1.5 an example set of ellipses is shown that conform to Eqn. 1.4 with $f = \pm 200$. It also shows all points x, y of the diffraction curve (Eqn. 1.5) for $a \in \mathbb{R}^+$.

1.2.3.2 Cone beam geometry

Now that we know the diffraction curve for the case where the source and detectors are located on the focal points of ellipses centred on the origin, we introduce a transformation such that each source, detector pair in volume coordinates is convert into ellipse coordinates such that these restrictions apply.

Given are a source point S and detector point D. The focal points, $\pm f$, of all ellipses is half the Euclidean distance between source and detector:

$$f = \frac{\|SD\|_2}{2} = \frac{1}{2} \sqrt{(D_x - S_x)^2 + (D_y - S_y)^2 + (D_z - S_z)^2}. \tag{1.7}$$

With f known, the source and detector points can be expressed in ellipse coordinates:

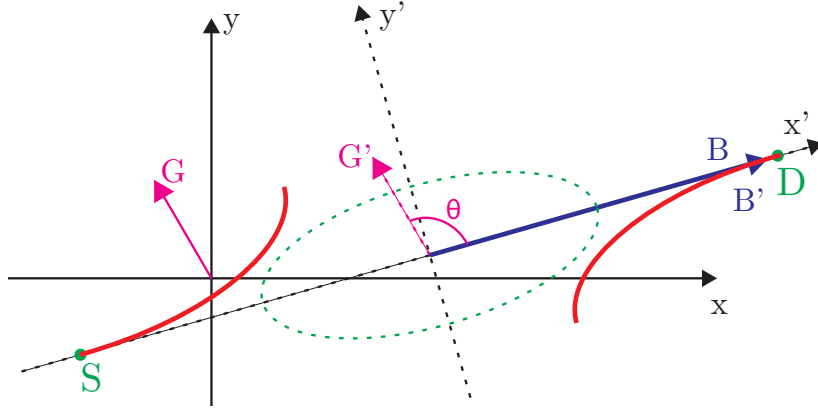$$S' = (-f, 0) \quad D' = (f, 0). \tag{1.8}$$

Figure 1.6: Two-dimensional simplification of the transformation between the a volume coordinates (full lines) and ellipse coordinates (dotted lines).

The plane normal in ellipse coordinates, G', can be described by the angle θ between G and the vector, B, from the halfway point between the source and the detector, to the detector (i.e. $B = D - \frac{S+D}{2} = \frac{S-D}{2}$). From the definition of the dot product, we learn that

$$\cos\theta = \frac{B \cdot G}{\|B\|\|G\|} = \frac{B \cdot G}{f}. \qquad \boxed{1.9}$$

Given $\sin^2\theta + \cos^2\theta = 1$, $\sin\theta$ can be also be computed without performing a costly trigonometric function. The plane normal in ellipse coordinates is thus:

$$G' = \left(g, \sqrt{1-g^2}\right), \quad \text{with } g = \frac{1}{f}\left(B_x G_x + B_y G_y + B_z G_z\right). \qquad \boxed{1.10}$$

If it is assumed that G' is not parallel to D' (which means the ray will never hit the detector anyway), the vectors G' and D' provide a basis for the ellipse coordinate system and each point P' can be described by a linear combination of these vectors:

$$\begin{aligned}
P' &= \alpha D' + \beta G' \\
P'_x &= \alpha f + \beta G'_x, \quad P'_y = \beta G'_y \\
\beta &= \frac{P'_y}{G'_y}, \quad \alpha = \frac{P'_x - \beta G'_x}{f}
\end{aligned} \qquad \boxed{1.11}$$

Furthermore, note that the transformation of G' and D' into volume coordinates (i.e. G and B) provides a basis for all diffraction points in volume coordinates with the origin at $O = \frac{S+D}{2}$. Because the transformation from ellipse to volume coordinates involves translation and rotation, but no scaling, the linear combination of these base vectors in the ellipse coordinate system is equal to the corresponding set of base vectors in the volume coordinate system, i.e.

$$P = O + \alpha B + \beta G. \qquad \boxed{1.12}$$

This means that we now have the means to transform the LabDCT projection of any source-detector pair into the simplified geometry of Section 1.2.3.1 (with Eqn. 1.10), where the diffraction curve can be easily computed. With Eqn. 1.12, this curve can be reconverted into the actual volume coordinates, leading to a forward projection.
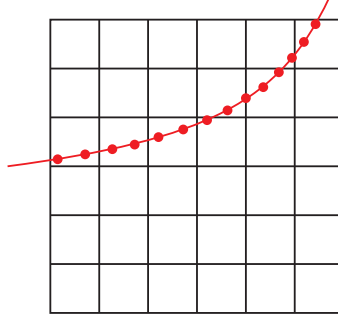
1.2.3.3 Sampling based projector

Figure 1.7: Scheme depicting a two-dimensional simplification of volume sampling along a certain diffraction curve.

Now that formulas for the diffraction curve are available, we can use them to create a ray-driven forward projection strategy. We have found that from a computational point of view, the best projection method is to sample the volume along the diffraction curve Eqn. 1.6 at a certain interval (see Fig. 1.7). With such methods, the sampling interval should be as regular as possible. In the case of the diffraction curve however, the derivative of the curve is not constant and if it were to be sampled with a fixed Δx or a fixed Δy, it is likely to be severely undersampled when its slope is very steep.

Instead, note that for each value of x (with $f < x < -|2fG_xG_y|$), a unique value of a can be associated, and that a increases as x increases (This is only true for $x < 0$. However, because we can assume that the reconstruction volume is much closer to the source than it is to the detector, the case where $x > 0$ can be ignored). One could thus also sample the curve by slowly increasing Δa, which offers a much more even sampling strategy. This has the added benefit that the projection can be computed using Eqn. 1.5, which is substantially more computationally efficient than Eqn. 1.6. [2]

Given $0 < a_0 \leq f$ a certain starting value, compute its corresponding point, P_0, on the diffraction curve. Next, add Δa to a_0 and compute its corresponding point P_1. Before P_1 is "looked" up in the volume image and added to the detector value, its weight has to be computed. This weight should be the inverse of the curve length between P_0 and P_1. Because it is not possible to compute this efficiently, one simplification can be to use the Euclidean distance between the two points. If Δa is chosen sufficiently small, this simplification should not result in large errors. Keep adding Δa to a and repeat the computations until the diffraction curve does not lie in the volume any more.

As an additional improvement, one can adaptively update Δa by dividing it by the distance between the last two points (i.e. the weight associated to the last point). This will ensure that the distance from this point to the next will be approximately equal to the distance between this point and the previous, obviously resulting in an a much smoother sampling of the curve.

In Fig. 1.8, the LabDCT forward projector is summarized in pseudo code.

1.2.3.4 Some optimizations

We have done research into the further improvement of the performance of the forward projection operation. We noticed that in the typical setup, the reconstruction volume lies much closer to the source than to the detector and is very small relative to the source detector distance. Furthermore, for grains to be visible on the detector plane, the plane normal of the projection is typically close to perpendicular to the incoming rays. This means that the curvature of the portion of the diffraction curve that falls inside the region of interest, is typically very low. We have thus found that the curve can be approximated with a straight line without a substantial loss in accuracy.

---

[2]Note that in Eqn. 1.6 the computational burden appears to lie mostly with the reciprocal square root. Fortunately, however, on nVidia GPU's the reciprocal square root is implemented as a hardware instruction, and thus requires only one clock cycle to compute.

$a := a_0$ such that P_0 lies inside the volume
$P'_{0x} := -a^2|G_x|/\sqrt{a^2 - f^2G_y^2};$ $P'_{0y} = -sgn(G_x)b^2|G_y|/\sqrt{a^2 - f^2G_y^2};$
$\beta := P'_{0y}/G'_y;$ $\alpha := (P'_{0x} - \beta G'_x)/f;$
$P_0 := O + \alpha B + \beta G;$
$a := a + \Delta a;$
while P_0 is inside the volume
   $P'_{1x} := -a^2|G_x|/\sqrt{a^2 - f^2G_y^2};$ $P'_{1y} = -sgn(G_x)b^2|G_y|/\sqrt{a^2 - f^2G_y^2};$
   $\beta := P'_{0y}/G'_y;$ $\alpha := (P'_{0x} - \beta G'_x)/f;$
   $P_1 := O + \alpha B + \beta G;$
   $w := \|P_1 - P_0\|_2;$
   $v :=$ lookup value of the volume at point $P_1;$
   $projection := projection + wv;$
   $P_0 := P_1;$
   $\Delta a := \Delta a/w;$ (optional)
   $a := a + \Delta a;$
end

Figure 1.8: Pseudo code for sampling-based LabDCT forward projector.

Assume that the grain falls entirely inside a sphere centred in point $C \in \mathbb{R}^2$ with radius $r \in \mathbb{R}$. One can then compute the intersection of this sphere with the diffraction curve Eqn. 1.5. One can then draw a straight line between these two points, sampling them at a fixed interval.

1.2.4 Implementation details

In this work, multiple implementations of the previously discussed projector were created. Initial prototyping development was done fully in MALTAB. Later on, a C++ implementation was created where the computational efficiency was optimized. In this, the inherent parallelism of the projectors was exploited with the OpenMP framework. To even further decrease the computation time, also an NVIDIA CUDA implementation was created. In it, parallelism is exploited even more ad GPU specific techniques such as texture memory are used to increase the speed of bicubic interpolation and random memory lookups.

Both the C++ and the CUDA versions are part of the ASTRA framework. For now, access to this code is restricted to the partners of this project. There is, however, the option to include these projectors in a future open source release of the ASTRA toolbox. At the time of writing, the code is already deployed on a computation cluster at the ESRF, Grenoble, France.

1.3 Experiment

For validation of the projector introduced in Section 1.2, we consider a experimental dataset acquired on the laboratory X-ray tomography setup at MATEIS, INSA Lyon. The instrument (manufacturer: RX Solutions, France) is equipped with a Hamamatsu microfocus X-ray source. The source was operated at 60 keV acceleration voltage and a 5μm thick tungsten transmission target. The images were recorded on a CCD detector (ESRF Frelon camera) featuring a 2048×2048 pixel array and a dynamic range of 14 bits. The backilluminated CCD sensor is fibre-optically coupled to a 100 m thick fluorescent screen (GadOx). The pixel size of the detector system was 50 microns. The centre of rotation of the tomographic rotation stage was positioned at a distance of 36 mm from the source and the detector was positioned at a distance of 220 mm from the source. This resulted in an effective pixel size of about 8 microns, taking into account the cone beam magnification. A set of adjustable slits were inserted between the sample and the source in order to limit direct X-ray exposure to the central part of the detector field of view (figure 1.2). Two scans were recorded from the same sample — a DCT scan optimized for detection of the weak diffraction signals and a conventional absorption scan. For the DCT scan, a 1 mm thick copper sheet was placed as an absorber over the area of the detector exposed to the direct beam, in order to
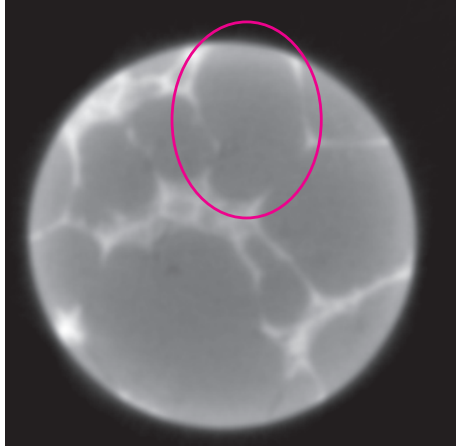
Figure 1.9: Slice of the absorption reconstruction of the AlCu dataset. Highlighted is the grain that is used in the subsequent experiments.

avoid saturation of the detector system.

The sample was made from a binary Al Cu alloy (5 weight percent copper) which was thermo-mechanically processed in a way to produce large Al grains (500 microns) partly surrounded by a copper rich Eutectic phase. A slice of the absorption reconstruction of this dataset is shown in Fig. 1.9.

One reason we chose this dataset is that the individual grains can be more or less seen in the absorption reconstruction, allowing us to create a manual three-dimensional segmentation of the grain shapes. Note that while it is tempting to refer to such a segmentation as a "ground truth", the fact that it was created by manually delineating the borders of the grain on a slice-by-slice basis, means that it should only be used as a rough guideline of the exact grain shape. A more accurate segmentation may be obtained using advanced morphological image segmentation techniques (watershed algorithm).

Following the procedure outlined in [4], a number of grains were identified (indexed) from the LabDCT dataset. In what follows, we describe two experiments that we did with the data from one of those grains which could be identified both in the absorption reconstruction (i.e. a grain delineated by the Eutectic phase) and indexed during processing of the diffraction data.

First, in Section 1.3.1, we show a reconstruction that we did of a phantom volume, based on the manually segmented grain volume. Secondly, in Section 1.3.2 we attempt to reconstruct the same grain, with the actual experiment data.

1.3.1 Phantom experiment

Firstly, we consider the manual segmentation we created of the grain highlighted in Fig. 1.9, a slice of which is shown in Fig. 1.10a. Of this volume, we simulated the diffraction spots with the same projection geometry (i.e. the same directions) as the experimentally recorded dataset. With this projection data, we computed a reconstruction, shown in Fig. 1.10b. As reconstruction algorithm, we used 50 iterations of SIRT with minimum constraints (i.e. after each SIRT iterations, all negative values in the reconstructed are put to zero).

While there are some clearly visible streaks in the reconstructed image, the general outline of the grain is reconstructed very well.

1.3.2 Real data experiment

Secondly, we created a SIRT reconstruction of the experimental data. This time, we opted for only 10 iterations, as we noticed a decreasing reconstruction quality when, due to noisy projection data, doing more iterations. A slice of the reconstruction is shown in Fig. 1.11b, where it is also compared
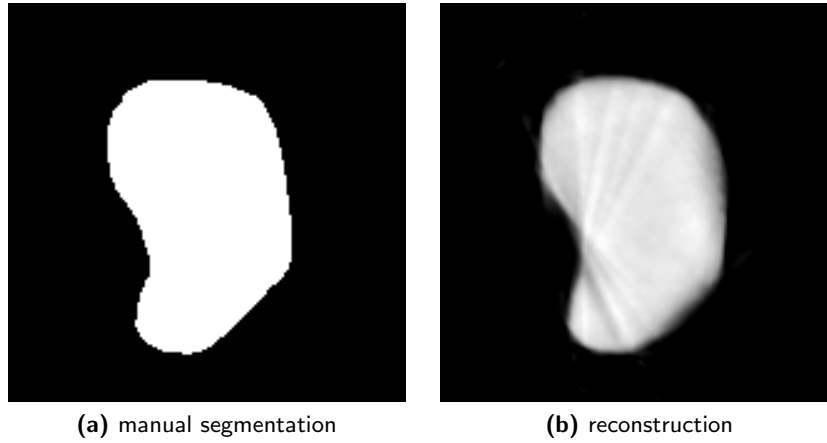
(a) manual segmentation   **(b)** reconstruction

Figure 1.10: (a) Slice of the manually segmented grain (Fig. 1.9) (b) Reconstruction of (a) computed from 162 simulated diffraction spots with the same geometry as the dataset of Fig. 1.9.
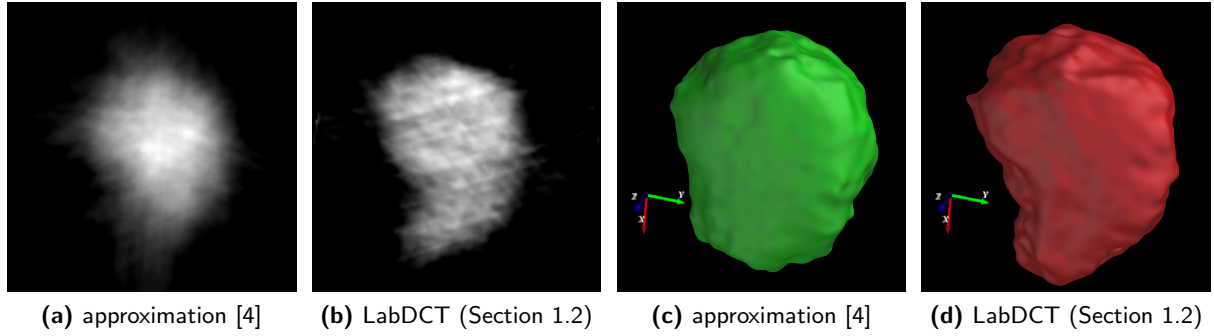

(a) approximation [4]   **(b)** LabDCT (Section 1.2)   **(c)** approximation [4]   **(d)** LabDCT (Section 1.2)

Figure 1.11: **(a)** Reconstruction slice with an approximated projector [4]. **(b)** Reconstruction slice with the projector introduced in Section 1.2. **(c,d)** Volume rendering of the full volumes of (a) and (b) respectively.

(Fig. 1.11a) to the reconstruction obtained with the previously published approach in which regular cone beam projectors were used and the diffraction geometry was approximated by some afffine transformation of the projection images [4].

Clearly, the method presented in this work much better approximates the shape of the grain as it is visual in the absorption reconstruction (Note that the shown slices in Fig. 1.11a, Fig. 1.11b and Fig. 1.9 are not exactly the same).

We also compared the computational efficiency of the different implementations of the projectors. In Fig. 1.12, timings are shown for the forward and backprojection and for a 10 iteration SIRT reconstruction. The computations were performed on an Intel Quad Core i7-2760 CPU running at 2.40GHz and on an NVIDIA Quadro 2000M GPU (note that this is only a laptop GPU, with a modern high end GPU we expect a further speedup by a factor of 2). An enormous computational improvement was obtained by implementing the projector in C++ instead of in MATLAB code. While this was indeed expected, it must be noted, however, that the MATLAB implementation is not fully optimized for speed and the comparison is thus unfair. Overall, however, it is clear that for the best performance, GPU computing is the way to go. With features such as fast texture interpolation and memory lookup, the GPU architecture is excellently suited for projectors such as ours, and vice versa.

implementation	FP	BP	SIRT (10 iters)
MATLAB	896.40s	2128.12s	32514.11s
C++	5.89s	28.10s	382.64s
CUDA	0.45s	0.69s	13.78s

Figure 1.12: Projection and reconstruction timings for the different implementations.

1.4 Outlook and conclusions

In this work we have developed an efficient projector for laboratory based, polychromatic cone beam diffraction imaging. Using this projector, the three-dimensional shape of grains with negligible intra-granular orientation gradient can be reconstructed using iterative, algebraic reconstruction techniques (e.g. SIRT). The reconstructions show a clear improvement compared to the previously used processing route, based on a regular cone beam projector and affine transformation of the projection images.

Further validation and evaluation of the new projector will become possible after sucessfull indexation of the majority of the grains in the illuminated sample volume - currently only about 40 percent of the sample volume has been indexed. Where this document only provides a visual confirmation of the accuracy (partly delineation of the grain boundaries by the Eutectic phase), quantiative evaluation will be possible after having scanned the same sample on a synchrotron beamline using the well established monochromatic, parallel beam approach.

We expect that further improvement of the reconstruction quality can be obtained from more accurate estimation of the projection geometry. Currently, the plane normals, defining the direction of the diffracted beam are derived from the orientation matrix, determined during the indexing procedure. Due to incertainties in the global setup parameters, this initial estimate of the orientation is not 100 percent accurate, which results in blurry reconstructions. This problem is closely related to projection misalignment, common to other applications such as electron tomography.

The logic continuation of the current work, aiming at further improvement of the grain shape reconstructions is along the following lines:

Grain refinement The initial estimate of grain center of mass position and orientation as provided by the indexing routine has to be refined. However, the refinement of grain parameters can only be successful if the global setup parameters like detector position and tilt of the rotation axis are refined at the same time. Therefore, a multiparameter fitting procedure, based on the full set of diffraction spot metadata is required (estimated time: 1-2 months for implementation and testing). Alternatively, grain reconstructions could be improved on a grain by grain basis. Recently, at the Vision Lab (Antwerp, Belgium), a state-of-the-art alignment correction method for tomography was developed (not yet published). We are confident that the underlying principles of this method can also be used to improve the plane normal estimations, which is likely to lead to sharper reconstructions of individual grains, albeit not solving the underlying problem of a slightly inaccurate initial position and orientation estimate of the grain.

Intragranular orientation gradients One of the principal limitations of polychromatic cone beam DCT is its restriction to materials exhibiting negligible levels of intragranular orientation spread. In the current work we have assumed that the direction of the diffracting plane normal is constant throughout the entire grain volume. In practise, this condition is rarely fulfilled and already small deviations of order of a few tenths of a degree of intragranular orientation spread can give rise to significant distortion of the diffraction spots and will lead to rapid degradation of the accurary of grain shape reconstructions. It can be expected that a 6-dimensional reconstruction framework, as currently developed for the case of monochromatic beam DCT [5], will be able to improve the quality LabDCT reconstructions, as well. Since this method is computationally expensive, the fast GPU implementation developed in the current work may be considered as a

prerequiste and first step in this direction. However, the polychromaticity of LabDCT implies that the additional information encoded into the ω (rotation angle) spead of the individual diffraction spots, observed in the monochroamtic beam variant, is lost. As a first step, the stability and applicability of such a 6-D reconstruction framework has to be tested on synthetic data created from a phantom grain with known orientation distribution. If successfull the application to real data and validation with cross-sectional EBSD and / or synchtrotron measurements can be envisaged. The time required for adapting the 6-dimensional reconstruction framework to LabDCT (creation of test cases, optimization of the algorithm and model , validation) is estimated to be of order of 6 months.

Source spectrum In this work, we have assumed that the polychromatic X-ray source has a constant energy spectrum. In practice this may not be the case and strong peaks (characteristic emission lines of the X-ray target material) can be present in the spectrum. This means that within a single diffraction spot, which typically covers a small range of different energies, the contribution from different grain sub-volumes may be highly non-uniform. Assuming the source spectrum is known a priori, one may attempt to extend the current projection model such that this non-constant spectrum is taken into account. While this is likely to decrease the computational efficiency of the projection, it may be beneficial to its accuracy. As first step, we intend to perform software simulations in order to evaluate the impact of the source spectrum on the reconstruction quality. If these simulations indicate a strong influence, we will proceed with the implementation of projectors and algorithms, taking this effect into account.

To summarize, we have implemented and validated a projector for LabDCT which enables us to perform accurate 3D grain shape reconstructions in materials exhibiting negligible intra-granular orientation spread. With further improvement of polycrystal indexing algorithms and with extension to a 6D reconstruction framework, we anticipate LabDCT to become a true alternative to established synchrotron techniques. The combination of absorption (detection of damage, second phases, porosity, plastic strain via 3D digital volume correlation techniques) and diffraction imaging (crystal shape and orientation, elastic strain) on the same instrument will provide unique possibilities for (interrupted) in-situ characterization of dynamic processes in the bulk of polycrystalline materials (e.g. grain coarsening during heat treatment, plastic deformation and damage mechanisms, others...)

References

[1] A. King, G. Johnson, D. Engelberg, W. Ludwig, and J. Marrow, "Observations of intergranular stress corrosion cracking in a grain-mapped polycrystal.," *Science*, vol. 321, no. 5887, pp. 382–385, 2008.

[2] M. Herbig, A. King, P. Reischig, H. Proudhon, E. M. Lauridsen, J. Marrow, J.-Y. Buffière, and W. Ludwig, "3d growth of a short fatigue crack within a polycrystalline microstructure studied using combined diffraction and phase contrast x-ray tomography," *Acta Materialia*, vol. 59, pp. 590–601, 2011.

[3] W. Ludwig, A. King, P. Reischig, M. Herbig, E. M. Lauridsen, S. Schmidt, H. Proudhon, S. Forest, P. Cloetens, S. R. d. Roscoat, J. Y. Buffière, T. Marrow, and H. F. Poulsen, "New opportunities for 3D materials science of polycrystalline materials at the micrometre lengthscale by combined use of X-ray diffraction and X-ray imaging," *Materials Science and Engineering: A*, vol. 524, pp. 69–76, 2009.

[4] A. King, P. Reischig, J. Adrien, and W. Ludwig, "First laboratory X-ray diffraction contrast tomography for grain mapping of polycrystals," *Journal of Applied Crystallography*, vol. 46, pp. 1734–1740, Dec 2013.

[5] N. Viganò, W. Ludwig, and K. J. Batenburg, "Reconstruction of local orientation in grains using a discrete representation of orientation space," *Journal of Applied Crystallography*, submitted.

2 Appendix

2.1 Backprojection

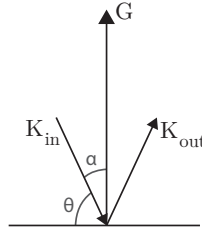### 2.1.1 Link to Bragg's law

Figure 2.1: Diffraction direction according to Bragg's law.

In DCT, the direction of the diffraction is defined by the Laue equation, which is equivalent to Braggs's Law:

$$G = K_{out} - K_{in}, \tag{2.1}$$

where $\|K_{out}\| = \|K_{in}\|$, and $\|K\| = 1$ (see Fig. 2.1). Here, we derive the equivalence to Eqn. 1.1. Given the incoming angle α, the norm of K_{out} and K_{in} can be easily found:

$$1 = \|G\| = 2\|K_{in}\|\cos\alpha = 2\|K_{in}\|\sin\theta,$$

$$\|K_{in}\| = \frac{1}{2\sin\theta}. \tag{2.2}$$

We then get:

$$\begin{aligned}
K_{out} &= 2G(G \cdot K_{in}) + K_{in} \\
&= 2G(\|G\|\|K_{in}\|\sin\theta) + K_{in} \\
&= 2G(\frac{1}{2\sin\theta}\sin\theta) + K_{in} \\
&= G + K_{in}
\end{aligned} \tag{2.3}$$

2.1.2 Solving Eqn 1.3

Given the equation $D_0 + t_1 U + t_2 V = P + sK_{out}$, here we discuss how to efficiently find $s, t1, t2 \in \mathbb{R}$. First, find s by computing the intersection between the line $P + sK_{out}$ and the detector plane:

$$s = \frac{(D_0 - P) \cdot N}{K_{out} \cdot N},$$

<div align="right">(2.4)</div>

where N is the normal to the detector plane, i.e. $N = U \times V$. Note that N can be precomputed for computational efficiency.

The value for $t1$ can subsequently be computed, depending on the value for U_x:

$$t_1 = \begin{cases} \frac{V_z(P_x - D_{0x} + sK_{out,x}) - V_x(P_z - D_{0z} + sK_{out,z})}{U_x V_z - U_z V_x} & \text{if } U_x \neq 0 \\ \frac{V_z(P_y - D_{0y} + sK_{out,y}) - V_y(P_z - D_{0z} + sK_{out,z})}{U_y V_z - U_z V_y} & \text{if } U_y \neq 0 \end{cases}.$$

<div align="right">(2.5)</div>

Note that we don't consider the case where $U_x = U_y = 0$. However, because U represents the unit vector for a column on the detector plane, we can assume that at least one of U_x and U_y is non-zero. For the same reason we can also assume that $V_z \neq 0$, leading to the following equation for t_2:

$$t_2 = \frac{P_z - D_{0z} + s * K_{out,z} - t1 * U_z}{V_z}$$

<div align="right">(2.6)</div>

2.2 Forward Projection, Ellipse model

Consider the set of ellipses with its center in the origin, their axes aligned with those of the Cartesian grid and with fixed focal points $\pm f$ with $f^2 = a^2 - b^2$ and $0 \leq b < a$.

$$\frac{x^2}{a^2} + \frac{y^2}{b^2} = 1.$$

<div align="right">(2.7)</div>

Given a certain point x_0, y_0 on such an ellipse, the slope of the tangent line of the ellipse at that point can be found by implicit differentiation along x:

$$b^2 x^2 + a^2 y^2 = a^2 b^2$$

$$\frac{d}{dx}\left(b^2 x^2 + a^2 + y(x)^2\right) = 0$$

$$2b^2 x + 2a^2 y \frac{dy}{dx} = 0.$$

The slope of the tangent line, m_t, is thus

$$m_t = \frac{dy}{dx} = -\frac{b^2}{a^2}\frac{x}{y}.$$

<div align="right">(2.8)</div>

We are now looking for points x_0, y_0 where the tangent line is perpendicular to the diffraction normal, whose slope is defined by $m_g = \frac{G_y}{G_x}$:

$$m_t m_g = -1$$

$$\frac{b^2}{a^2}\frac{x_0}{y_0}\frac{G_y}{G_x} = 1$$

<div align="right">**14**</div>

This gives rise to a line through the origin, that intersects the ellipse exactly at the two points where its tangent curve is perpendicular to the normal vector:

$$a^2 G_x y = b^2 G_y x$$
$$y = \frac{b^2}{a^2} \frac{G_y}{G_x} x = \frac{b^2}{a^2} m_g x \tag{2.9}$$

Now, given a certain x_0, we wish to know y_0 for which the previous equations hold. This can be done by computing the intersection between Eqn. 2.9 and the ellipse Eqn. 2.7, which is[1]:

$$x_0 = \pm \frac{ab}{\sqrt{a^2 \frac{b^4 m_g^2}{a^4} + b^2}} = \pm \frac{a}{\sqrt{\frac{b^2 m_g^2}{a^2} + 1}} = \pm \frac{a}{\sqrt{m_g^2 - \frac{f^2 m_g^2}{a^2} + 1}} = \pm \frac{a}{\sqrt{\frac{1}{G_x^2} - \frac{G_y^2 f^2}{G_x^2 a^2}}} = \pm \frac{a^2 |G_x|}{\sqrt{a^2 - f^2 G_y^2}}, \tag{2.10}$$

$$y_0 = \pm \frac{ab}{\sqrt{a^2 \frac{b^4 m_g^2}{a^4} + b^2}} \frac{b^2}{a^2} m_g = \pm \frac{a^2 b^2 |G_x| G_y}{G_x a^2 \sqrt{a^2 - f^2 G_y^2}} = \pm \frac{\mathrm{sgn}(G_x) b^2 G_y}{\sqrt{a^2 - f^2 G_y^2}}. \tag{2.11}$$

Given that the volume will always lie much closer to the source than to the detector, we are only interested in points for which $x_0 < 0$. Thus,

$$\gamma = -\frac{1}{\sqrt{a^2 - f^2 G_y^2}}, \quad x_0 = a^2 |G_x| \gamma, \quad y_0 = \mathrm{sgn}(G_x) G_y (f^2 - a^2) \gamma. \tag{2.12}$$

With x_0 given and b easily computable with $b^2 = a^2 - f^2$, Eqn. 2.12 can be solved for the two remaining unknowns (y_0 and a). From Eqn. 2.10, a^2 can be found:

$$x_0^2 = \frac{a^4 G_x^2}{a^2 - f^2 G_y^2}$$
$$0 = G_x^2 a^4 - x_0^2 a^2 + f^2 G_y^2 x_0^2$$

Solving for a^2, one gets

$$a^2 = \frac{1}{2 G_x^2} \left(x_0^2 \pm x_0 \sqrt{x_0^2 - 4 G_x^2 G_y^2 f^2} \right). \tag{2.13}$$

With a^2 known and $b^2 = a^2 - f^2$, Eqn. 2.9 can be used to represent the diffraction curve y_0 as a function of x_0:

$$y_0 = \frac{b^2}{a^2} m_g x_0 = m_g x_0 - \frac{f^2}{a^2} m_g x_0$$
$$= \frac{G_y}{G_x} x_0 - \frac{f^2 G_y x_0}{\frac{1}{2 G_x^2} \left(x_0^2 \pm x_0 \sqrt{x_0^2 - 4 G_x^2 G_y^2 f^2} \right) G_x}$$
$$= \frac{G_y}{G_x} x_0 - \frac{2 f^2 G_x G_y}{x_0 \pm \sqrt{x_0^2 - 4 f^2 G_x^2 G_y^2}}. \tag{2.14}$$

It should be noted that if

$$x_0^2 < 4 f^2 G_x^2 G_y^2 \iff |x_0| < |2 f G_x G_y|, \tag{2.15}$$

---

[1] http://mathworld.wolfram.com/Ellipse-LineIntersection.html

a^2 will be a complex number, meaning that for these x_0 values, no ellipse exists where the tangent slope at x_0 is perpendicular to G. This property can be used to define limits to where the curve should be computed.

Also note that both Eqn. 2.12 and Eqn. 2.13 feature $\frac{1}{G_x}$. This is a potential cause for severe floating point errors if G_x is very small. In that case, the plane normal is close to perpendicular to the incoming ray and the diffraction will be infinitesimally small.